

# Broadcasting Convolutional Network

Simyung Chang<sup>1,2</sup>, John Yang<sup>1</sup>, SeongUk Park<sup>1</sup>, Nojun Kwak<sup>1</sup>

<sup>1</sup>Graduate School of Convergence Science and Technology, Seoul National University

<sup>2</sup>Samsung Electronics

{timelighter, yjohn, swpark0703, nojunk}@snu.ac.kr

## Abstract

*While convolutional neural networks (CNNs) are widely used for handling spatio-temporal scenes, there exist limitations in reasoning relations among spatial features caused by their inherent structures, which have been issued consistently in many studies. In this paper, we propose Broadcasting Convolutional Networks (BCN) that allow global receptive fields to share spatial information. BCNs are simple network modules that collect effective spatial features, embed location informations and broadcast them to the entire feature maps without much additional computational cost. This method gains great improvements in feature localization problems through efficiently extending the receptive fields, and can easily be implemented within any structure of CNNs. We further utilize BCN to propose Multi-Relational Networks (multiRN) that greatly improve existing Relation Networks (RNs). In pixel-based relation reasoning problems, multiRN with BCNs implanted extends the concept of ‘pairwise relations’ from conventional RNs to ‘multiple relations’ by relating each object with multiple objects at once and not in pairs. This yields in  $\mathcal{O}(n)$  complexity for  $n$  number of objects, which is a vast computational gain from RNs that take  $\mathcal{O}(n^2)$ . Through experiments, BCNs are proven for their usability on relation reasoning problems, which is due from their efficient handlings of spatial information.*

the receptive fields are mapped with convolution filters at fixed areas, which derives CNNs to disregard spatial locations when encoding optimal features. They require either a bigger size of filters that embrace multiple input entities or repetitive usage of smaller filters in deeper networks in order to learn spatial relationships. Yet, it seems clear that CNNs show limited performance in any large deformation of input as long as the scope of convolution or pooling filters stay local and small-sized [5, 12, 13, 22, 24, 27].

The core of relational reasoning instrumentally depends on spatial learning [3, 26], and relational networks (RNs) [25, 27] have fostered the performance vastly on related tasks based on their spatial grid features. However, assuming each grid represents object features at the corresponding position within the scene, the computation of object pairs, while ordering matters, gets more expensive as the number of objects,  $n$ , increases. Thus, the method is hard to be implemented in large networks.

As a general solution to maximizing the spatial information control efficiency while minimizing the computational cost, we propose two methods: 1. Broadcasting convolutional networks (BCN) that overcome conventional limitations of CNNs by broadcasting all effective spatial features on every receptive fields. 2. BCN-based Multi-relational networks (multiRN) that outperforms conventional RNs in both performance and computational expense. Our approach focuses on modularizing our simple network which can be included in any structure of CNNs for training without complex implementation techniques and control strategies.

The paper is organized as follows. In Section 2, related works to our proposed method are reviewed. Section 3 explains the structures of BCN. The BCN-based multiRN, which can be effectively used for pixel-based relational reasoning by using BCN, is proposed in Section 4. We show the efficiency of our proposed methods quantitatively and qualitatively through experiments in Section 5 and finally, Section 6 provides conclusions.

## 1. Introduction

A complete cognizance of a visual scene can be achieved with the relational reasonings of a set of detected entities in an attempt to discover the underlying structure of them [18]. Reasoning comparative relationships allows artificial intelligence to infer semantic similarities or transitive orders among objects in scenes with various perspectives and scales [5, 25, 27].

While convolutional neural networks (CNNs) [21] have allowed success in many computer vision problems [7, 19, 23, 11, 6], they still suffer from difficulties in generalization over geometric variations of scenes. This is mainly because

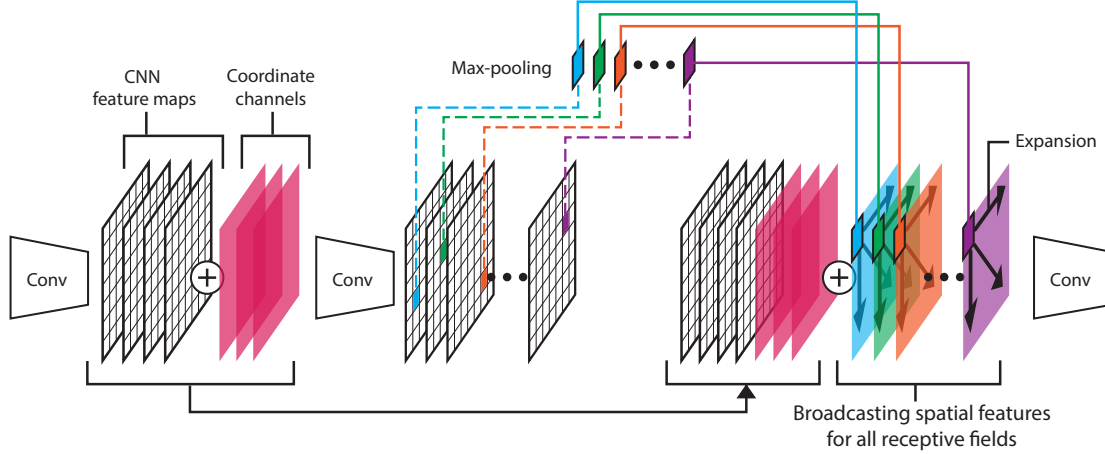


Figure 1: **Broadcasting Convolutional Network Modules.**  $N$  feature maps acquired from previous convolution layers are concatenated with coordinate planes during CCE phase. Then, additional light-weight convolution layer(s) (e.g. two layers of  $1 \times 1$  convolution with ReLU activation) is(are) operated. An  $1 \times 1 \times n$  vector is generated by max-pooling from each filter channel of the resultant feature maps. The vector is then expanded to emulate the size of the original feature maps, and merged with the original feature maps as an input to the next layer of convolution.

## 2. Related Works

Our motif has two aspects : 1. condensing and extracting dynamic spatial features, 2. projecting them to effective receptive fields, which are demanded by multi-scale reasonings and full resolution dense relational predictions.

Many previous computer vision related researches have used pooling techniques for extracting meaningful spatial features [4]. Spatial pyramid pooling [8] uses manual control over pooling scales and regional features are extracted from variations of hand-engineered pooling scopes. This issue has been developed in [14] where a large set of various pooling bins are initiated and the algorithm learns to select sparse subset of them. These works take hand-crafted pooling regions that cannot be learned end-to-end.

ROI pooling structure [5, 4] is similar to our method’s in a way of executing pooling methods in channel-wise. Each channel represents feature maps from starting stride point to last, and thus may possess objective spatial features. However, with conventional ROI pooling methods, each feature map does not reflect any relations among feature maps.

Features in multi-location can be conveniently condensed through max-pooling in our network. A similar approach was done in SENET [11] where they propose a module that squeezes and excites the original outputs of convolution filters. The feature maps get ‘squeezed’ by average-pooling and are fed into a shallow MLP network to re-learn the weights in order to rescale and ‘excite’ the original feature channels. Since the target of SENET is to perform better in visual classification problems such as ImageNet [6], their average-pooling is purely for generalization of fea-

tures. The theory of average-pooling is fundamentally contrary to our intention because the spatial features that we look for get dimmed by taking global mean-value and thus the network loses positional features. SENETs are not able to digest any regional information and poorly perform in finding locale relationships among objects within a scene.

In our method, the max-pooled features are condensed with noticeable features with positional information due to previous convolution layer(s) of which inputs are concatenated with coordinate information so they can be projected to the whole space of original feature maps for further relational convolution operations.

While effective receptive field size is previously known to increase linearly with the number of convolutional layers [24], the works in [5] have found that it actually increases with square root of the number of layers which is a much slower rate. This finding further leads to a logical doubt that deep CNNs may never have large enough receptive field size even at top layers. This phenomenon is prominent in fully convolutional networks (FCNs) with a large input image. To overcome the issue, large enough receptive field size is not the only aspect that is essential but the the learning of its flexibility depending upon situations, which explains why atrous convolution methods are used widely.

Deformable convolutional neural networks (Deformable ConvNet) [5] propose deformable convolution that learns the applicable filters with adaptive receptive fields. Their convolution filters are chained with offset parameters which represent the mapping of the original receptive fields to unique and irregularly dispersed receptive fields from each

spatial location. The offset parameters are optimized along with the convolutional filters during back-propagation. They, as their primitive motivation, further emphasize the importance of adaptive receptive learning in the needs of effectively computing large enough receptive fields at the top layers [24]. However, Deformable ConvNets require extra computation upon original CNNs, and their feature map sampling method in a local manner hinders themselves from having complete spatial support.

Other atrous convolution usages include increasing the receptive field size by sampling from dilated sparse regions [10]. This allows to retain the same computational complexity as previous CNNs' while increasing receptive field sizes, and thus is widely used in semantic segmentation problems [23, 1, 30]. If depth conditions are excluded, the method is still doubted on utilizing enough size of receptive fields. Our model handles extracted convolutional features by projecting them to global receptive fields, intending to convolve the features from various spatial spaces with the original features in all receptive fields.

The proposed BCN looks similar to skip-connections [28]. In addition to the aspects of convolving features with those from previous layers, BCN broadcasts spatial information in channels that can be convolved together. It is empirically shown in a later section that existing skip-connections improve ordinary CNNs, but not as much as BCNs do.

### 3. Broadcasting Convolutional network

In this section, we will first describe the overall architecture of BCN with details of our implementations and their purposes.

#### 3.1. Broadcasting ConvNet

The Broadcasting Convolutional Networks are applied after each pixel of the feature maps acquires a proper size of receptive fields through basic convolutions. Figure 1 describes how a BCN module can be applied to the conventional CNNs. The proposed BCN mainly consists of four components: 1) coordinate channel embedding (CCE), 2) plain convolutions of a few layers, 3) a global max-pooling layer, and then 4) the broadcasting phase.

Our method concentrates on reusing the relationship among current positional features and broadcasting them to global receptive fields during further convolution operations. Concatenating extracted features with the original feature maps, the network can compare the objective positional features (CCE) and the relative positional features (broadcast features).

We first make feature maps that represent the coordinate information and concatenate them with the original CNN feature maps. Then, rather simple convolution operations

(e.g. a few layers of  $1 \times 1$  convolution with ReLU activation) are applied, which is followed by a global max-pooling stage. Let us say that a feature map in the shape of  $h \times w \times n$  is generated from previous convolution operations, where  $n$  is the number of filters and  $h$  and  $w$  represent height and width of the feature maps produced, respectively. In this sense, a maximum element can be extracted from each filters so that an  $1 \times 1 \times n$  vector is generated. The feature vector is then expanded to emulate the same size of the original feature maps, and then merged with the original feature maps to be convolutionally mapped together.

The whole structure of BCN can be succinctly described in an equation as

$$BCN(F, C, n) = \{C, \mathcal{E}(\max(\mathcal{CV}(\{F, C\}), n)), h, w\}. \quad (1)$$

Here,  $F \in \mathbb{R}^{h \times w \times n'}$  is the input feature map for the broadcast convolution module,  $C \in \mathbb{R}^{h \times w \times n_c}$  is  $n_c$  coordinate planes,  $n$  is the number of filters in the last layer of successive convolution operations which are collectively denoted by the operator  $\mathcal{CV}$ . The max operation is taken for each of  $n$  output feature maps of  $\mathcal{CV}$  such that it results in an  $1 \times 1 \times n$  vector.  $\mathcal{E}$  denotes an expansion operation which copies its input vector to the entire  $h \times w$  positions. The proposed BCN outputs a broadcast feature map  $B \in \mathbb{R}^{h \times w \times (n+n_c)}$ .

The convolution layer(s) right after the CCE phase can be one or multiple, however the major purpose of its(their) presence is to first generate abstract representations based on locations. This allows the further convolutional mappings in the later process to infer relative positions among features with the implanted information on the objective positions. In this paper, we have implemented two or three layers of  $1 \times 1$  convolution after CCE for all experiments to watch each pixel in feature maps being convolved depth-wise with undissolved coordinate information. Additionally, the number of feature maps has kept fairly small so that the coordinate planes can be adequately reflected to the outputs after convolution operations. Yet, the number of coordinates planes can apparently be increased according to one's taste if needed.

This simple setting allows massive improvement on efficiency of extracting and utilizing spatial features in CNNs without much additional computation.

#### 3.2. Coordinate Channel Embedding

Since CNNs have performed generalization by taking advantage of sharing convolutional kernels in all input locations, their consequential structures are difficult to conserve spatial information throughout the layers. One of the intuitive ways to reflect location information to filtered outputs is to embed unique coordinates along with the input.

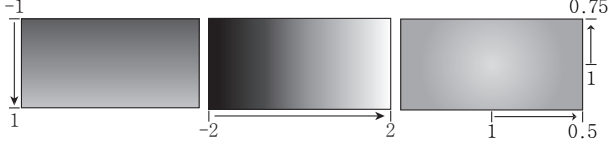


Figure 2: An example of coordinate planes,  $c_x$ ,  $c_y$  and  $c_r$ , for feature maps with 2:1 aspect ratio of width to height. The brighter, the higher value.

In our method, the feature location information is implanted in original feature maps as additional channels as shown in Figure 1. This specific decision comes from the motivation to assign objective positional components to each feature during convolutions before the max-pooling phase, and to establish relative location for the comparison against other spatial features when broadcasting. This allows additional convolutional mappings to reflect the feature positions when generating higher level features.

The coordinates are embedded in three different planes; one for the x-axis,  $c_x$ , another for the y-axis,  $c_y$  and the last one for the radial distance from center,  $c_r$ . Since inputs of our module may not necessarily have the shape of square, elements of each plane are normalized as follows :

$$\begin{aligned} s_c &= \min(\text{width}, \text{height})/2 \\ s_p &= \max(\text{width}, \text{height}) * 2 \\ \bar{x} &= (\text{width} - 1)/2 \\ \bar{y} &= (\text{height} - 1)/2 \\ c_x[:, x] &= (x - \bar{x})/s_c \quad \forall x \in X \\ c_y[y, :] &= (y - \bar{y})/s_c \quad \forall y \in Y \\ c_r[y, x] &= 1 - d_c(x, y)/s_p \quad \forall x, y \in X, Y, \end{aligned}$$

where  $X$  and  $Y$  refer to a set of pixel positions in corresponding axes, and  $\bar{x}$  and  $\bar{y}$  refer center points of the planes.  $d_c(x, y)$  is the distance of  $(y, x)$  from the center  $(\bar{y}, \bar{x})$ .

It can be seen that the Cartesian coordinates  $c_x$  and  $c_y$  tend to be zero towards the center. This prevents features from being biased near bottom right-side which occurs if coordinates near top left start from zero as used in usual computer graphics. An additional radial coordinate plane removes any bias caused by having a comparably low absolute value at the center and provides distance information from the center. Also, when inputs with different aspect ratio are given, initial values in CCE are scaled to cope with the different aspect ratio. This scaling yields CCE invariant to those kind of inputs.

#### 4. Multi-Relational Networks

Visuospatial tasks necessitate recognition of relevant features from the spatial organization of stimuli and selection of stimulus that matches one or more of these identi-

fied features [3, 26]. Algorithms such as relational networks (RNs) [25, 27] have introduced solutions for relational reasoning problems including CLEVR dataset [15] based on their spatial grid features – the dataset is explained in a more detailed manner later in this paper. Utilizing BCN, RNs can be greatly improved in both performance and computational efficiency.

In [27], an RN module for a set of  $n$  objects,  $O = \{o_1, \dots, o_n\}$ , is introduced, which consists of two functions  $f_\phi$  and  $g_\theta$  such that :

$$\mathcal{RN}(O) = f_\phi\left(\sum_i \sum_j g_\theta(o_i, o_j)\right), \quad (2)$$

where  $f_\phi$  represents MLP operations on the visuospatial relation features that have been generated by another MLP operation  $g_\theta$  from all pairwise combinations of objects. The ‘relations’ are the outputs of  $\mathcal{O}(n^2)$  time of computations from  $g_\theta$ . Earlier in this paper, we have explained how BCN allows multiple spatial features to be represented in one dimensional vector. With the help of BCN denoted by (1), original RN in (2) can be revised into Multi-Relational Networks (multiRN) as follows:

$$\text{multiRN}(O) = f_\phi\left(\sum_i g_\theta(o_i, \mathcal{BCN}(O))\right). \quad (3)$$

Since  $\mathcal{BCN}(O)$  connotes multi-location features for multiple objects, each object feature can be paired with multiple object location features, fed into  $g_\theta$  and computed in  $\mathcal{O}(n)$ . This allows not only exponential gain in computation complexity but also relational comparison with multiple objects at once. The outputs of  $g_\theta$  should, in our context, be redefined as ‘multiple relations’, and can be trained end-to-end to convey information about how much of certain object feature at particular location should be reflected for visual relational reasoning.

Furthermore, the number of objects,  $n$ , in pixel-based relational reasoning problems is defined by  $n = h \times w$  where  $h, w$  are height and width of resultant 3-dimensional tensors from previous convolution layers. Such trait allows us to replace the MLP operation for  $g_\theta$  in RNs with  $1 \times 1$  convolution after channel concatenations of BCN outputs as shown in Figure 3. The non-pixel-based objects such as questions in visual question and answering (VQA) problems can be additionally concatenated in channels. The final form of our multi-relational network is :

$$\text{multiRN}(O) = f_\phi\left(\sum_i g_\theta(o_i, \mathcal{BCN}(O), \text{question})\right). \quad (4)$$

In practice, *questions* are expanded for channel embedding, and the final tensor is fed into  $g_\theta$ -convolution operations to achieve ‘multiple relations’.



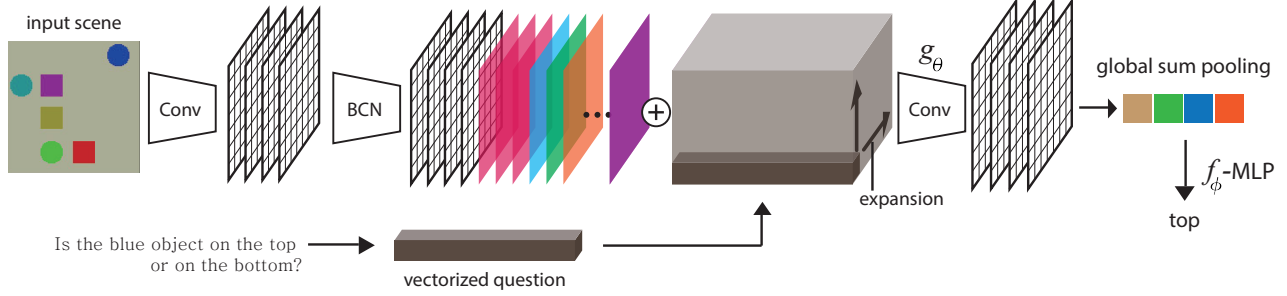


Figure 3: **Multi-Relational Networks.** For visual relational reasoning problems, input scenes are fed into ordinary convolutional layers and a BCN module. Questions about the input scene are mapped to unique vectors and expanded to emulate the size of BCN outputs. As it can be seen above, each question vector is projected in all receptive fields. Since the outputs of BCNs connote visuospatial features of multiple objects, they can be merged with the expanded question tensor for further convolution operations,  $g_\theta$ . Then, global sum poolings are operated on feature maps produced, and the outcomes are integrated to answer questions.

## 5. Experiments

The proposed method has been tested in several experiments and it is compared with other similar methods to verify the effectiveness of BCN and MultiRN. The purposes of the experiments are to prove the efficiency of our methods by answering to the following questions : (1) can BCN not only improve the representation power of features but also enhance the localization performance? (2) how effective is MultiRN on pixel-based relational reasoning problems? (3) do our methods effectively extend the receptive fields globally to adaptively learn the relationships of key spatial features? and (4) why does the coordinate channel embedding method work?

### 5.1. Tasks

We have experimented our methods on four datasets, Scaled-MNIST, STL-10, Sort-of-CLEVR with pixels, and CLEVR with pixels, for different purposes.

**Scaled-MNIST** dataset is our own remodeled version of original MNIST dataset [20]. Locating the original MNIST of size  $28 \times 28$  to  $128 \times 128$  image space, we randomly scale the width irregularly ranging from 28 to 105 pixels and the aspect ratio as 1:0.8 to 1:1.2. All digits are positioned randomly within the image space, avoiding being cropped by edges. Along with the class labels, another label is added for the locations of center points for each digit in order to evaluate localization performance of the models.

**STL-10** [2] is a classification dataset motivated from CIFAR-10 dataset. It is a set of natural image with ten class labels each of which has 500 training images and 800 test images. There are also unlabeled images within the dataset, but we do not use them because experiments on them are irrelevant to our intentions. The data consists of images sized in  $96 \times 96$  with higher resolution than those of CIFAR-10 but less number of training images.

**CLEVR with pixels** [15] is one of visual QA datasets. This

is a challenging problem set requiring high-level relational reasonings. The dataset contains images of 3-D rendered objects and corresponding questions asking about several attributes of the objects. We have experimented only on the pixel version of the CLEVR dataset whose images are represented in 2-D pixel-wise.

**Sort-of-CLEVR with pixels** [27] is our main experiment for multiRN. Sort-of-CLEVR is a more simplified version of CLEVR, which is a set of images combined with caption dataset for relation and non-relation reasoning. Each image contains six of differently colored 2-D geometric shapes, and corresponding 20 questions; 10 for relational and 10 for non-relational reasonings. Questions in this dataset are already vectorized, and thus the experiments are independent from any additional vector embedding models, which allows more reasonable comparison based on the results.

### 5.2. Experiment Settings

For all experiments, BCN uses multiple convolution layers with different size of  $1 \times 1$  kernel and ReLU for non-linearity. The number of filters in  $m$  convolution layers for a BCN is written in the form of  $[S_1, \dots, S_m]$  in each experiment.

**Scaled-MNIST** : As a baseline model, we assign a convolution layer with 24 of  $3 \times 3$  kernels, stride size of two and padding size of one for each edge, followed by a ReLU activation function and a batch normalization. We have stacked three to five of these convolutional layers depending on the experiments. This setting is purposefully designed to compare performance of a simpler model with BCN against that of baseline model with more depths on the given data. For the top layers of the networks, we use global average pooling layer paired with two kinds of linear layers; one with ten output nodes using softmax unit which predicts classification outputs, and another with two output nodes whose output predicts center coordinates (x, y). A BCN with size

| Model                                 | Classification Acc. | Localization Err. | Number of Parameters | Runtime <sup>1</sup> |
|---------------------------------------|---------------------|-------------------|----------------------|----------------------|
| Baseline                              | 84.4%               | 0.151             | 11.2K                | 4.5ms                |
| Baseline(depth 4)                     | 94.9%               | 0.149             | 16.5K                | 5.1ms                |
| Baseline(depth 5)                     | 96.4%               | 0.089             | 21.9K                | 5.5ms                |
| Baseline(depth 5, $2 \times$ filters) | 97.2%               | 0.077             | 85.2K                | 8.5ms                |
| Base + Deformable Conv [5]            | 90.8%               | 0.087             | 32.0K                | 582.9ms              |
| Base + Dilated Conv [30]              | 91.0%               | 0.152             | 11.2K                | 4.7ms                |
| Base + Skip-Connection                | 87.0%               | 0.151             | 29.0K                | 8.4ms                |
| Base + Skip-Connection + CCE          | 87.9%               | 0.071             | 29.2K                | 8.41ms               |
| <b>Base + BCN</b>                     | <b>97.5%</b>        | <b>0.023</b>      | 29.2K                | 8.41ms               |

Table 1: **Results on Scaled MNIST.** Skip-Connection denotes using the shape of BCN without CCE, global max-pooling and broadcasting, and only operates  $1 \times 1$  convolution and concatenating. This can be viewed just the same as skip-connection [28].

of [64, 64, 128] is applied once in between the second and third layers. After applying the BCN, the number of feature maps increases, so in order to match the input dimension of the third layer,  $1 \times 1$  convolutions are operated for dimension reduction to 24.

With the same baseline model (a CNN with three layers), experiments of deformable convolutions and dilated convolutions are also done. The deformable convolution layers are applied to all three layers, and the dilated convolution layer is applied in the second layer of the baseline model with  $2 \times 2$  dilation.

**STL-10 :** For a baseline model for the STL-10 dataset, four layers of convolutions with 64 of  $3 \times 3$  kernels with stride size of two and padding size of one for each edge are applied. A ReLU activation function and a batch normalizing operation follow after each convolution layer. A BCN module of size [128, 128, 256] is applied in between third and fourth layers. After applying the BCN module, the number of feature maps increases, so in order to match the input dimension of fourth layer, an  $1 \times 1$  convolution layer is used for dimension reduction to 64. In addition, we have applied the same size of BCN to a Resnet18 model [9]. Since the input image size of STL-10 images is  $64 \times 64$ , kernel sizes in the very first convolutional layer are modified from  $7 \times 7$  to  $3 \times 3$  while max pooling layers are eliminated. The BCN module within the Resnet18 model is applied between third and fourth residual blocks. Then, 256 of  $1 \times 1$  convolution filters are used to reduce number of feature maps, and the entire model is trained end-to-end from scratch.

**Sort-of-CLEVR with pixels :** There are two versions of complete relational networks suggested in [27]; a network tested on Sort-of-CLEVR and a smaller network tested on CLEVR. In our experiment, both networks are tested on Sort-of-CLEVR dataset as baseline models. Our reproduced relational networks used for Sort-of-CLEVR and CLEVR from [27] are respectively denoted as 'RN\*' and 'RN<sub>c</sub>' in Table 3. The main structure of multiRN replicates that of RN<sub>c</sub> except that  $g_\theta$  is changed with BCN whose size is [128, 128, 256] and additional two convolution layers with 256, 256  $1 \times 1$  kernels, ReLU non-linearities, and  $f_\phi$  is set up

with two layers of MLP both consisting of 256 units with ReLU.

Also, in terms of verification of the hypothesis that multiRNs use computation resource efficiently, we changed fourth convolution layer's stride from 2 to 1 in the multiRN<sup>+</sup> network, which makes input feature map size from  $5 \times 5$  to  $10 \times 10$  and quadruples the number of objects that the following network has to handle. This allows more detailed spatial feature extractions of BCN but results in more object feature comparisons needed during multiRN. The same condition has been made on an RN<sub>c</sub> module and experimented, denoted as 'RN<sub>c</sub><sup>+</sup>' in Table 3.

**CLEVR :** An experiment has been done on a more challenging relational reasoning problem to test the performance of multiRN compared to existing RNs. Our reproduced RN module for CLEVR dataset, denoted as 'CNN+LSTM+RN\*' in Table 4, is replicated, having internal RN module replaced with multiRN. The structure of multiRN model is the same as it was used for Sort-of-CLEVR dataset, and question vectors are generated from an LSTM model which is also implemented in original RN modules.

### 5.3. Quantitative Analysis

**Scaled-MNIST:** Table 1 shows the performance enhancement of both classification and localization results on Scaled-MNIST datasets. The baseline achieves 97.8% accuracy in the original MNIST, but the performance of the scaled MNIST decreases as the size of the required receptive field increases. Making the model deeper to extend the receptive field usually achieves better performance. The gap between the performance of baseline model (convolutional network with depth 3) with skip-connection and that of the same network with CCE verifies the effectiveness of coordinate channel embedding. Also, comparing the baseline model with skip-connection and CCE against the baseline with BCN verifies the effectiveness of broadcasting spatial

<sup>1</sup>All runtimes are measured on Nvidia Titan X (Pascal) GPU and 8 core CPU(i7-6700K) per 100 samples.

| Model                      | Accuracy      | #Params | Runtime <sup>1</sup> |
|----------------------------|---------------|---------|----------------------|
| Tho17-2 Single [29]        | 75.76%        | 1.46M   | -                    |
| Tho17-2 Ensemble [29]      | 78.66%        | 1.46M   | -                    |
| Baseline                   | 68.75%        | 114K    | 18.1ms               |
| Baseline + Skip-connection | 69.79%        | 192.7K  | 18.2ms               |
| <b>Baseline + BCN</b>      | <b>72.18%</b> | 193.2K  | 18.2ms               |
| Resnet18                   | 76.27%        | 11.2M   | 102.2ms              |
| <b>Resnet18 + BCN</b>      | <b>77.00%</b> | 11.46M  | 105.5ms              |

Table 2: **Results on STL-10.** All models are trained from scratch without any external dataset.

| Model                        | Relational     | Non-relational | #Params      | Runtime <sup>1</sup> |
|------------------------------|----------------|----------------|--------------|----------------------|
| RN                           | 94% $\uparrow$ | 94% $\uparrow$ | 19.5M        | -                    |
| RN*                          | 91.0%          | 99.6%          | 19.5M        | 575.8ms              |
| RN <sub>c</sub>              | 89.9%          | 99.8%          | 36.5K        | 23.5ms               |
| RN <sub>c</sub> <sup>+</sup> | 96.5%          | 99.9%          | 36.5K        | 315.6ms              |
| <b>multiRN</b>               | 92.9%          | 99.8%          | <b>34.5K</b> | <b>8.3ms</b>         |
| <b>multiRN<sup>+</sup></b>   | <b>96.7%</b>   | <b>99.9%</b>   | <b>34.5K</b> | 9.9ms                |

Table 3: **Results on Sort-of-CLEVR.** The performance of RN is reported in [27], and RN\* is the reproduced result with same model. RN<sub>c</sub> use the model of CLEVR in [27]. <sup>+</sup> denotes the model that has 1 stride for fourth convolution layer instead of 2 stride to handle more objects.

| Model                          | Overall     | Count | Exist | Compare Numbers | Query Attribute | Compare Attribute |
|--------------------------------|-------------|-------|-------|-----------------|-----------------|-------------------|
| Human                          | 92.6        | 86.7  | 96.6  | 86.5            | 95.0            | 96.0              |
| Q-type baseline                | 41.8        | 34.6  | 50.2  | 51.0            | 36.0            | 51.3              |
| LSTM                           | 46.8        | 41.7  | 61.1  | 69.8            | 36.8            | 51.8              |
| C+LSTM                         | 52.3        | 43.7  | 65.2  | 67.1            | 49.3            | 53.0              |
| C+L+SA                         | 68.5        | 52.2  | 71.1  | 73.5            | 85.3            | 52.3              |
| C+L+RN                         | 95.5        | 90.1  | 97.8  | 93.6            | 97.9            | 97.1              |
| C+L+RN*                        | 90.9        | 86.7  | 97.4  | 90.0            | 90.2            | 93.5              |
| <b>C+L+multiRN</b>             | 92.3        | 85.2  | 96.5  | 93.6            | 95.1            | 92.9              |
| <b>C+L+multiRN<sup>+</sup></b> | <b>97.2</b> | 94.1  | 98.9  | 98.3            | 98.6            | 97.6              |

Table 4: **Results on CLEVR.** The performance of our model and previously published results [16][27]. RN\* is the result when we reproduce the same model as the paper. (C+L = CNN+LSTM)

features in all receptive fields. Even if we increase the receptive field with depth of convolution layer up to five, we can see that our method with only depth of three performs better than the conventional CNN of depth five by 1.1 %. The model with BCN even shows better performance than doubling the number of filters in the baseline by 0.3%.

Since the goal of deformable convolutions are similar to ours in many ways, and it has also showed desirable results, getting better score on both classification and localization. Dilated convolutions model has resulted in impressive improvement in classification accuracy while conserving the same parameter numbers and computation speed as those of the baseline. Nonetheless, the performance of BCN model is better than that of both models with deformable convolution and dilated convolution.

**STL-10 :** We compare our model with baseline model in Table 2 to evaluate the performance of BCN in natural image

classifications. Because BCN has potential of growing receptive field size to whole image pixels, it allows 3.4% performance enhancement from the baseline model. Also, this was a better result compared to the model without broadcasting and coordinate channel embedding, which has the same network structure as BCN.

The additional experiment where BCN is applied within the Resnet18 model shows that our approach sets a new state-of-the-art performance in STL-10 experiment on a single network basis with 77.0%, which is 1.24% higher than single model of Tho17-2 [29].

**Sort-of-CLEVR:** Result of Table 3 suggests that using our version of RN (multiRN) is better than the conventional RN (RN<sub>c</sub>) at reasoning relations by 3%, which is the main job of sort of CLEVR task, despite of comparably fewer number of parameters.

When incrementing object features from  $5 \times 5$  to  $10 \times 10$ , the multiRN<sup>+</sup> performs better than other networks because the network handles finer spatial object features. Moreover, computation time is  $\mathcal{O}(n)$ , which has advantage over RN whose computation time is  $\mathcal{O}(n^2)$ . While the multiRN<sup>+</sup>'s computation cost is quadrupled (25 to 100) from multiRN, RN<sub>c</sub><sup>+</sup> takes 16 times greater computation loads (625 to 10000) than RN<sub>c</sub>. Both RN<sub>c</sub><sup>+</sup> and multiRN<sup>+</sup> have achieved impressive performance gain with increase in the number of feature objects. The final results show that the multiRN<sup>+</sup> outperforms all other variations of models and achieves the state-of-the-art performance.

**CLEVR:** The results of the comparative experiments on CLEVR are shown in Table 4. The RN\*, our reproduced version of the relational network from [27], has not been able to achieve the same performance as in the paper due to lack of original version's details of hyper-parameters and additional network control factors. However, since the input convolutional feature maps and question vectors are generated with the same CNN + LSTM settings, reasonable comparisons can still be made among the candidate methods. For this problem, our implementation using multiRN performs 1.4% better than RN\*, and multiRN<sup>+</sup> performs even far better with an achievement of 6.3% performance enhancement. This is an impressive result considering that the same CNN+LSTM+RN model architecture is used as in RN\* and allows 95.5% of performance whilst both of multiRN and multiRN<sup>+</sup> require a much smaller amount of computation. We have not been able to proceed an experiment with the RN<sup>+</sup> model because of the out-of-memory problem when dealing with an increased number of objects.

## 5.4. Qualitative Analysis

**Ability of BCN to embed pixelwise abstraction:** For better understanding of our model, we visualized the activation maps for different images of each experiment. Activation maps are acquired by unsampling the global maxpool-



Figure 4: **Activation map** shows how much information is broadcasted at each location. From top to bottom are Scaled MNIST, STL-10, Sort-of-CLEVR and CLEVR. The activation maps for the dataset Sort-of-CLEVR and CLEVR show that multiRN activates spatial features from given input feature maps to answer *questions*.

ing layer, and simply masking the pixel as 1 from where it was chosen. The number of masks is the same as the number of  $1 \times 1$  convolution filters, and summing them through feature dimension outputs the activation map. Figure 4 is activation maps of our experiments. In activation maps for Scaled MNIST, plotted at Figure 4, we can intuitively find that the activation map corresponds well with each digit’s location in the original image. The scaled-MNIST dataset may have too many zero inputs for a network to easily respond to spatial features, but activation maps in STL-10 apparently show that BCN makes abstractions of features well even in natural images. Notably, we could apparently observe that activation maps tend to draw features from important locations, such as edges, faces, legs and so on. For sort of CLEVR task and CLEVR task, we can obviously see that BCN is well trained to make abstractions of each object in their image. Note that since activation maps only represent the maxpooled features, it does not have to include all objects by themselves. Output convolution features that are inputted to the BCN module, which will be further com-

| Method  | Accuracy     | Localization err. |
|---|--------------|-------------------|
| No coordinates channel                                    | 92.5%        | 0.151             |
| X,Y Coordinates with top-left zero                        | 96.9%        | 0.029             |
| X,Y Coordinates with zero center                          | <b>97.5%</b> | 0.025             |
| <b>X,Y Coordinates with zero center + Radial distance</b> | <b>97.5%</b> | <b>0.023</b>      |

Table 5: Results on Coordinates Methods in Scaled MNIST

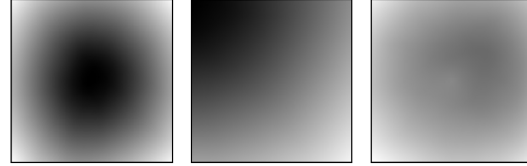


Figure 5: The output of coordinate planes through the convolution kernel. Left: X,Y Coordinates with zero center. Center: X,Y Coordinates with top-left zero. Right: X,Y Coordinates with zero center and additional Radial channel.

bin with BCN output, also contain features of objects.

**Study on coordinates:** Our demonstration on the effects of coordinate channels is shown in Table 8. The result without coordinate channels has far less score compared to the result with the coordinate channels embedded. The implementation of only two coordinate planes biased in x and y axes yields the same accuracy as that of three planes with extra radial distance plane included, but performs slightly worse in localization. This result can be interpreted in two ways: adding one channel as CCE improves localization because the weight of CCE in whole feature dimension gets larger, or radial coordinate channel embedding works better with the network.

Figure 5 shows the absolute values of the output from the convolution kernel with randomly initialized weights passing through the coordinate channels. As shown, a coordinate system with a conventional top-left of zero is deflected diagonally, but a coordinate system with zero center is deflected to the outside. On the other hand, by adding coordinate channels with radial distances, it can be seen that most of the deflection can be removed while providing coordinate information.

As shown in Table 8 and Figure 5, if coordinate planes are defined with diagonally biased elements and not zero-centered, outputs can be critically influenced in such way planes tend to excite the initialized features. Furthermore, although we have expected better feature representation and localization performance by concatenating an additional coordinate plane and reducing initial weight bias, the performance gain has only occurred in the localization aspect. This evidently implies that convolution operations are inherently biased towards the center with Gaussian distribution [24], and thus the additional coordinate plane have not been a critical catalyst.



## 6. Conclusion

We have shown that utilizing Broadcasting Convolutional Network (BCN) allows conventional CNNs to effectively collect and represent spatial information with efficient extension of receptive fields, which results in remarkable performance on localization problems. With BCN's ability of representing compounded spatial features in all receptive fields, we have proposed Multi-Relational Networks that greatly improve RN [27] in terms of computational gains while achieving state-of-the-art performance in pixel-based relation reasoning problems.

## References

- [1] L.-C. Chen, G. Papandreou, I. Kokkinos, K. Murphy, and A. L. Yuille. Deeplab: Semantic image segmentation with deep convolutional nets, atrous convolution, and fully connected crfs. *arXiv preprint arXiv:1606.00915*, 2016. 3
- [2] A. Coates, A. Ng, and H. Lee. An analysis of single-layer networks in unsupervised feature learning. In *Proceedings of the fourteenth international conference on artificial intelligence and statistics*, pages 215–223, 2011. 5
- [3] E. A. Crone, C. Wendelken, L. Van Leijenhorst, R. D. Honomichl, K. Christoff, and S. A. Bunge. Neurocognitive development of relational reasoning. *Developmental science*, 12(1):55–66, 2009. 1, 4
- [4] J. Dai, Y. Li, K. He, and J. Sun. R-fcn: Object detection via region-based fully convolutional networks. In *Advances in neural information processing systems*, pages 379–387, 2016. 2
- [5] J. Dai, H. Qi, Y. Xiong, Y. Li, G. Zhang, H. Hu, and Y. Wei. Deformable convolutional networks. *arXiv preprint arXiv:1703.06211*, 2017. 1, 2, 6, 12
- [6] J. Deng, W. Dong, R. Socher, L.-J. Li, K. Li, and L. Fei-Fei. ImageNet: A Large-Scale Hierarchical Image Database. In *CVPR09*, 2009. 1, 2
- [7] R. Girshick, J. Donahue, T. Darrell, and J. Malik. Rich feature hierarchies for accurate object detection and semantic segmentation. In *Proceedings of the IEEE conference on computer vision and pattern recognition*, pages 580–587, 2014. 1
- [8] K. He, X. Zhang, S. Ren, and J. Sun. Spatial pyramid pooling in deep convolutional networks for visual recognition. In *European Conference on Computer Vision*, pages 346–361. Springer, 2014. 2
- [9] K. He, X. Zhang, S. Ren, and J. Sun. Deep residual learning for image recognition. In *Proceedings of the IEEE conference on computer vision and pattern recognition*, pages 770–778, 2016. 6
- [10] M. Holschneider, R. Kronland-Martinet, J. Morlet, and P. Tchamitchian. A real-time algorithm for signal analysis with the help of the wavelet transform. In *Wavelets*, pages 286–297. Springer, 1990. 3
- [11] J. Hu, L. Shen, and G. Sun. Squeeze-and-excitation networks. *arXiv preprint arXiv:1709.01507*, 2017. 1, 2
- [12] M. Jaderberg, K. Simonyan, A. Zisserman, et al. Spatial transformer networks. In *Advances in Neural Information Processing Systems*, pages 2017–2025, 2015. 1
- [13] Y. Jeon and J. Kim. Active convolution: Learning the shape of convolution for image classification. *arXiv preprint arXiv:1703.09076*, 2017. 1
- [14] Y. Jia, C. Huang, and T. Darrell. Beyond spatial pyramids: Receptive field learning for pooled image features. In *Computer Vision and Pattern Recognition (CVPR), 2012 IEEE Conference on*, pages 3370–3377. IEEE, 2012. 2
- [15] J. Johnson, B. Hariharan, L. van der Maaten, L. Fei-Fei, C. L. Zitnick, and R. Girshick. Clevr: A diagnostic dataset for compositional language and elementary visual reasoning. *arXiv preprint arXiv:1612.06890*, 2016. 4, 5
- [16] J. Johnson, B. Hariharan, L. van der Maaten, J. Hoffman, L. Fei-Fei, C. L. Zitnick, and R. Girshick. Inferring and executing programs for visual reasoning. *arXiv preprint arXiv:1705.03633*, 2017. 7
- [17] M. Kågebäck and H. Salomonsson. Word sense disambiguation using a bidirectional lstm. *arXiv preprint arXiv:1606.03568*, 2016. 11
- [18] C. Kemp and J. B. Tenenbaum. The discovery of structural form. *Proceedings of the National Academy of Sciences*, 105(31):10687–10692, 2008. 1
- [19] A. Krizhevsky, I. Sutskever, and G. E. Hinton. Imagenet classification with deep convolutional neural networks. In *Advances in neural information processing systems*, pages 1097–1105, 2012. 1
- [20] Y. LeCun. The mnist database of handwritten digits. <http://yann.lecun.com/exdb/mnist/>, 1998. 5
- [21] Y. LeCun, Y. Bengio, et al. Convolutional networks for images, speech, and time series. *The handbook of brain theory and neural networks*, 3361(10):1995, 1995. 1
- [22] G. D. Logan and D. D. Sadler. A computational analysis of the apprehension of spatial relations. 1996. 1
- [23] J. Long, E. Shelhamer, and T. Darrell. Fully convolutional networks for semantic segmentation. In *Proceedings of the IEEE Conference on Computer Vision and Pattern Recognition*, pages 3431–3440, 2015. 1, 3
- [24] W. Luo, Y. Li, R. Urtasun, and R. Zemel. Understanding the effective receptive field in deep convolutional neural networks. In *Advances in Neural Information Processing Systems*, pages 4898–4906, 2016. 1, 2, 3, 8
- [25] D. Raposo, A. Santoro, D. Barrett, R. Pascanu, T. Lillicrap, and P. Battaglia. Discovering objects and their relations from entangled scene representations. *arXiv preprint arXiv:1702.05068*, 2017. 1, 4
- [26] J. C. Raven. Standardization of progressive matrices, 1938. *Psychology and Psychotherapy: Theory, Research and Practice*, 19(1):137–150, 1941. 1, 4
- [27] A. Santoro, D. Raposo, D. G. Barrett, M. Malinowski, R. Pascanu, P. Battaglia, and T. Lillicrap. A simple neural network module for relational reasoning. *arXiv preprint arXiv:1706.01427*, 2017. 1, 4, 5, 6, 7, 9, 11, 12
- [28] R. K. Srivastava, K. Greff, and J. Schmidhuber. Training very deep networks. In *Advances in neural information processing systems*, pages 2377–2385, 2015. 3, 6

- [29] M. Thoma. Analysis and optimization of convolutional neural network architectures. *arXiv preprint arXiv:1707.09725*, 2017. 7
- [30] F. Yu and V. Koltun. Multi-scale context aggregation by dilated convolutions. *arXiv preprint arXiv:1511.07122*, 2015. 3, 6, 12

## 7. Appendix

### 7.1. Experiment details

For the ease of reproduction of our experiment results, this section explains as much details as possible of our experiments. We used Pytorch of version 0.2.0.

#### 7.1.1 Scaled-MNIST

Scaled-MNIST dataset is created one time and has stayed stationary during training, and no further transformations are done, being restricted from aspects of data augmentation throughout our experiments. The models are optimized with the stochastic gradient descent method with learning rates of 0.01 during first 10 epochs, 0.001 during next 10 epochs and 0.0001 during last 10 epochs. However, the network using deformable convolutions have empirically required much more sensitive control during training. We therefore have heuristically chosen the learning rate of 0.00007 to avoid the over-fitting. All models are trained for 30 epochs and early-stopped because almost all of the experimented models become saturated before reaching 30 epochs. Our loss function is composed of two different loss functions both of which are weighted equally; the loss function for classification that computes negative log likelihood cross-entropy with softmax outputs and the loss function for localization with mean square error functions for the center location of digits.

#### 7.1.2 STL-10

In experiments of STL-10 classification dataset, a stochastic gradient descent optimizer is used and the learning rate is set as 0.1 during 10 epochs. The learning rate is controlled to get diminished by a factor of 0.1 in every additional 30 epochs until 200 epochs. We have augmented the original images with the size of  $96 \times 96$  by adding paddings of 4, randomly cropping them into the size of  $96 \times 96$  again, and normalizing RGB channels with the factors of mean, (0.4914, 0.4822, 0.4465), and variance, (0.2023, 0.1994, 0.2010). The same loss function for classification is used as in the experiments on ScaledMNIST dataset.

#### 7.1.3 Sort-of-CLEVR

For sort of CLEVR dataset, we have vectorized question data so that we do not have to deal with additional LSTM training. We use original images sized in  $75 \times 75$  without performing any augmentations. The candidate models are optimized with ADAM optimizers with learning rates of 0.001 during first 20 epochs and 0.0001 during next 30 epochs. We have early-stopped the training when the training reaches 50 epochs.

#### 7.1.4 CLEVR

Unlike Sort-of-CLEVR dataset, an additional LSTM model that vectorizes questions is also needed to be trained together while training end-to-end for CLEVR dataset. An ADAM optimizer is used with a learning rate of 0.00025 during first 200 epochs and 0.000025 during next 200 epochs. And, we use a single GPU with a batch size of 64 instead of the 10-distributed computing method performed in [27]. Optimizing the LSTM model parameters is a much difficult job without a weight decay factor because of training instability, and thus weight decay rate of 0.0001 is also applied. The LSTM model is structured with two layers of 128 bi-directional hidden units, taking pre-trained GloVe[17] embeddings with six billion tokens and 50-dimensional vectors

### 7.2. Additional Experiments

#### 7.2.1 Different Poolings

While max-poolings take a core part in our method when extracting and summarizing spatial features, we have also further experimented on average-pooling to see clear comparisons. Earlier this paper, we have explained our intention on avoiding mean-pooling, and the results empirically verify our assumption. In this part, we have experimented two same BCN models with an exception of the pooling style difference on the Scaled-MNIST dataset. The results are shown in Table 6. Implemented in a BCN model, max-pooling not only reduces the localization error, but also better performs in the classification tasks.

|              | Classification Accuracy | Localization Error |
|--------------|-------------------------|--------------------|
| mean-pooling | 92.7%                   | 0.064              |
| max-pooling  | 97.5%                   | 0.023              |

Table 6: Results of different pooling styles on Scaled-MNIST.

### 7.2.2 Robustness against Deformations

Previously introduced experiments on Scaled-MNIST are performed using the networks trained to minimize the hybrid loss function consisting of two terms: classification error (softmax classifier with cross-entropy cost) and localization error (distance error from the target center points). In order to objectively demonstrate the classification performance of BCN on the **Scaled-MNIST** dataset, the experiments were repeated with a single classification loss implementation.

While conventional approaches of feature generalization in computer vision tasks include data augmentation, invariant feature design, and other additional hand-crafted engineerings of feature representations, these attempts do not compromise robustness against geometric deformations of visual scenes. Globally broadcasting spatial features in all receptive fields, our method achieves spatial invariance against deformations in scales and rotations.

In a newly generated dataset, **MoreScaled-MNIST**, we have located the original MNIST dataset ( $28 \times 28$ ) randomly within  $256 \times 192$  image space while scaling the width of the original digit image from 28 to 160 pixels and the aspect ratio as 1:0.8 to 1:1.2 with uniform randomness. This dataset has not seen by the models during training, and is used solely for testing. All models are optimized through reducing classification loss. Additional to the scale deformations, we have tested two cases of rotation ( $\pm 10^\circ, \pm 45^\circ$ ) applied on each MoreScaled-MNIST image. **affNIST**<sup>2</sup>, lastly, is also tested. affNIST consists of original MNIST images with various reasonable affine transformations applied. The same models trained for the classification experiment on Scaled-MNIST dataset are tested on affNIST, MoreScaled-MNIST and its rotated versions without any additional training and data augmentation. The results are self-explanatory in Table 7. And Figure 6 depicts activation maps showing broadcasted information of MoreScaled-MNIST images with random rotations within a range of  $\pm 45^\circ$ . Mispredicted images are red-boxed with target labels pointing at predicted labels at the right side of bottom. Since the test images are scaled larger and rotated, the model with BCN tends to predict circinate digits as zero labels.

|                                      | Classification Accuracy |                  |                     |                     |              |
|--------------------------------------|-------------------------|------------------|---------------------|---------------------|--------------|
|                                      | Scaled-MNIST            | MoreScaled-MNIST | with $\pm 10^\circ$ | with $\pm 45^\circ$ | affNIST      |
| Baseline                             | 85.4%                   | 19.0%            | 20.0%               | 19.7%               | 27.9%        |
| Baseline(depth 4)                    | 95.6%                   | 53.4%            | 52.1%               | 41.6%               | 61.0%        |
| Baseline(depth 5)                    | 96.6%                   | 71.3%            | 69.2%               | 52.2%               | 77.4%        |
| Baseline(depth 5, $2 \times$ filter) | <b>97.5%</b>            | 88.5%            | 86.9%               | 65.2%               | 78.8%        |
| Base + deformable Conv [5]           | 93.0%                   | 27.9%            | 28.3%               | 25.6%               | 29.2%        |
| Base + dilated Conv [30]             | 90.5%                   | 27.0%            | 28.0%               | 25.3%               | 29.3%        |
| <b>Base + BCN</b>                    | 97.2%                   | <b>94.8%</b>     | <b>92.7%</b>        | <b>76.1%</b>        | <b>91.6%</b> |

Table 7: **Robustness against Deformation on Scaled MNIST**. The results of the networks with dilated convolutions and deformable convolutions may not necessarily represent the performances of their algorithms because the models we have experimented are modularized versions of their proposed concepts.

### 7.2.3 multiRN with different CCE

Concatenations of coordinate planes greatly improve the performance of multiRN, which can be shown in Table 8. Additional radial distance plane enhances the overall performance even more.

### 7.2.4 Sectional Runtimes

For an explicit comparison of computations performance, we have measured floating point operations on sectional parts of four networks,  $RN_c$  from [27],  $RN_c^+$ , multiRN and multiRN<sup>+</sup>. Changing the stride of the last convolution layer results in the change in the feature map size from  $5 \times 5$  to  $10 \times 10$ . Applying the stride size of 1 instead of 2 as in  $RN_c$  is denoted as  $RN_c^+$

<sup>2</sup><http://www.cs.toronto.edu/tijmen/affNIST/>



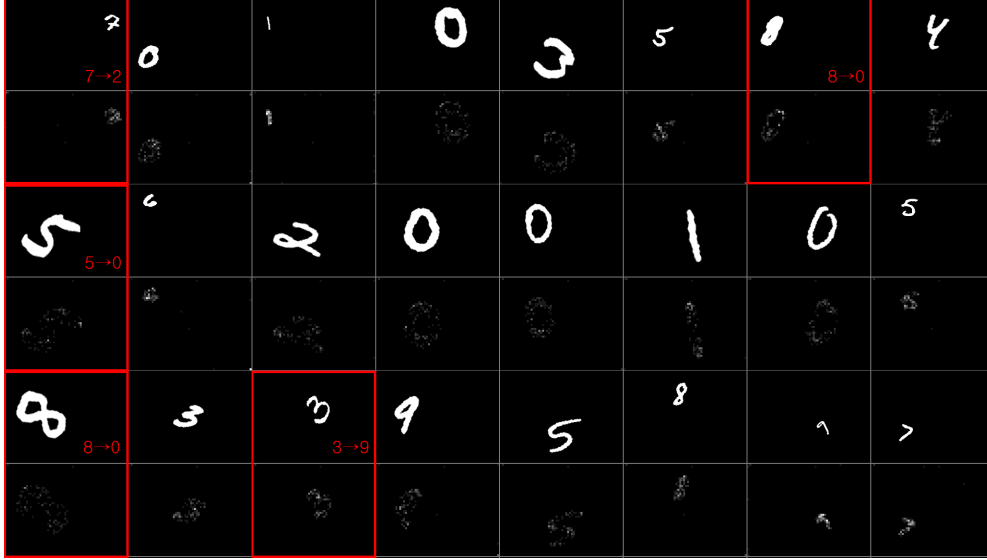


Figure 6: Comparison of activation maps for MoreScaled-MNIST with maximum of  $\pm 45^\circ$  rotation. Red-boxed figures are the misclassified digits with Base + BCN.

| Method  | Relational   | Non-Relational |
|---|--------------|----------------|
| No coordinates channel  | 91.4%        | 91.8%          |
| X,Y Coordinates with top-left zero                            | 92.6%        | 99.9%          |
| X,Y Coordinates with zero center                              | 96.1%        | 99.9%          |
| <b>X,Y Coordinates with zero center<br/>+ Radial distance</b> | <b>96.7%</b> | 99.9%          |

Table 8: Results on Coordinates Methods in Sort of CLEVR

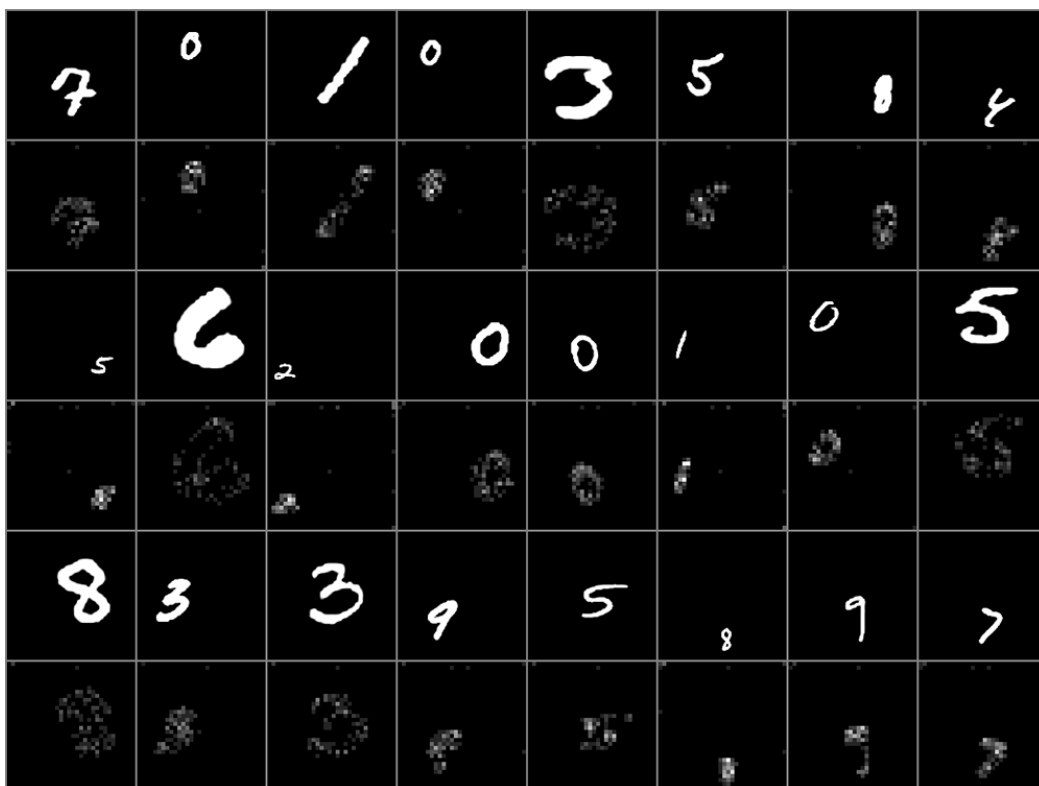
in Table 9 and the same application is done for  $\text{multiRN}^+$ . While the MLP operation of  $g_\theta$  in  $\text{RN}_c^+$  requires 16 times more of floating point operations after increasing feature map size four times larger than  $\text{RN}_c$ , the section of convolving the outputs after broadcasting requires just six times more of operations after increasing feature map size the same amount, which implies linear increments along the size of feature maps. Table 9 shows the extravagant computation cost gaps in total FLOPs among different methods. It shows huge computational saving of our method compared to RN.

|                      | Input Convolution | BCN    | $\sum g_\theta$ | $f_\phi$ | Total FLOPs |
|----------------------|-------------------|--------|-----------------|----------|-------------|
| $\text{RN}_c$        | 3.60M             | -      | 133.76M         | 133.4K   | 137.49M     |
| $\text{RN}_c^+$      | 3.98M             | -      | 2.26G           | 133.4K   | 2.26G       |
| multiRN              | 3.60M             | 3.22M  | 1.67M           | 133.4K   | 8.62M       |
| multiRN <sup>+</sup> | 3.98M             | 12.87M | 6.62M           | 133.4K   | 23.60M      |

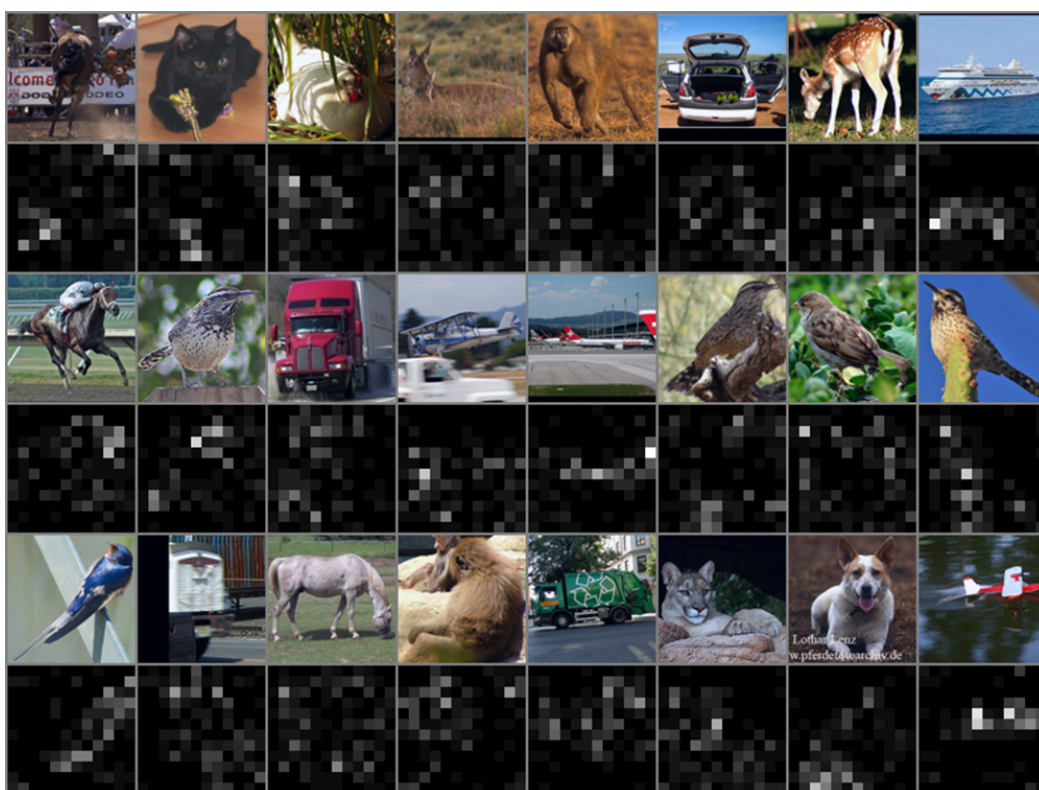
Table 9: Comparison of the number of FLOPs on Sort of CLEVR. Input convolutions and  $f_\phi$  are the same, but BCN and different  $g_\theta$  is implemented in multiRN

### 7.3. More Activation Maps

Figure 7 and Figure 8 are additional activation maps for the tasks tested in the paper. These are randomly selected samples to present how BCN learns to broadcast effective spatial features. The brighter parts indicate spatial locations where more information is broadcasted.

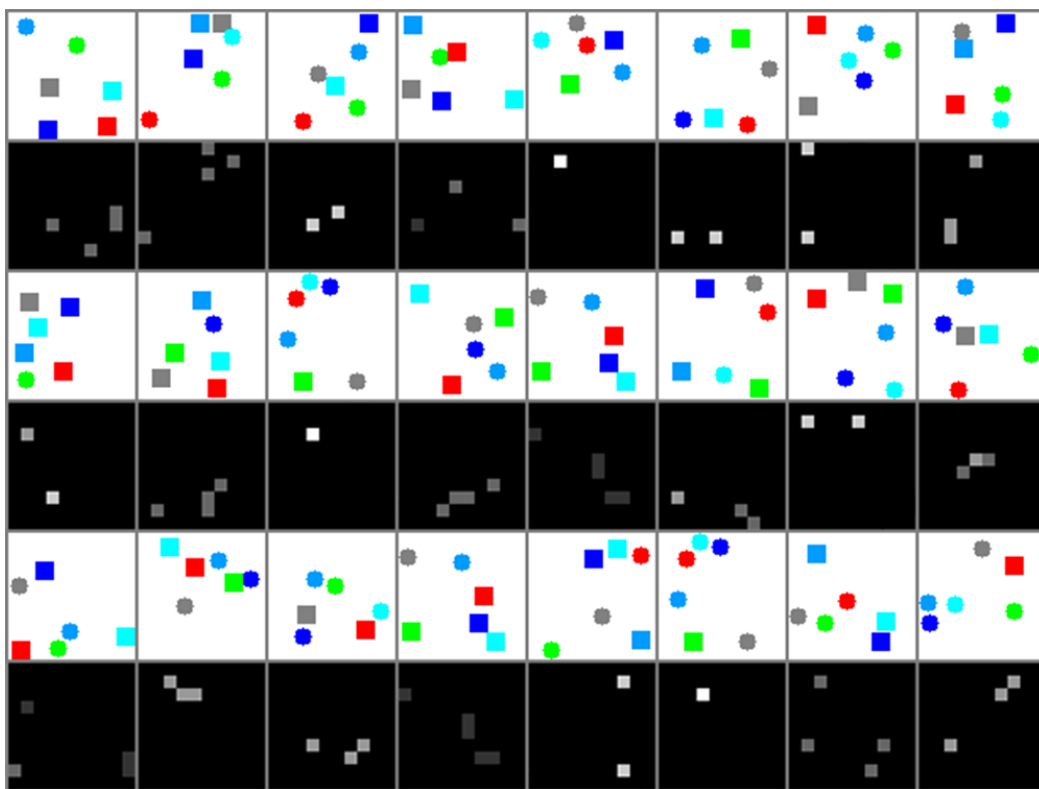


(a) Scaled MNIST

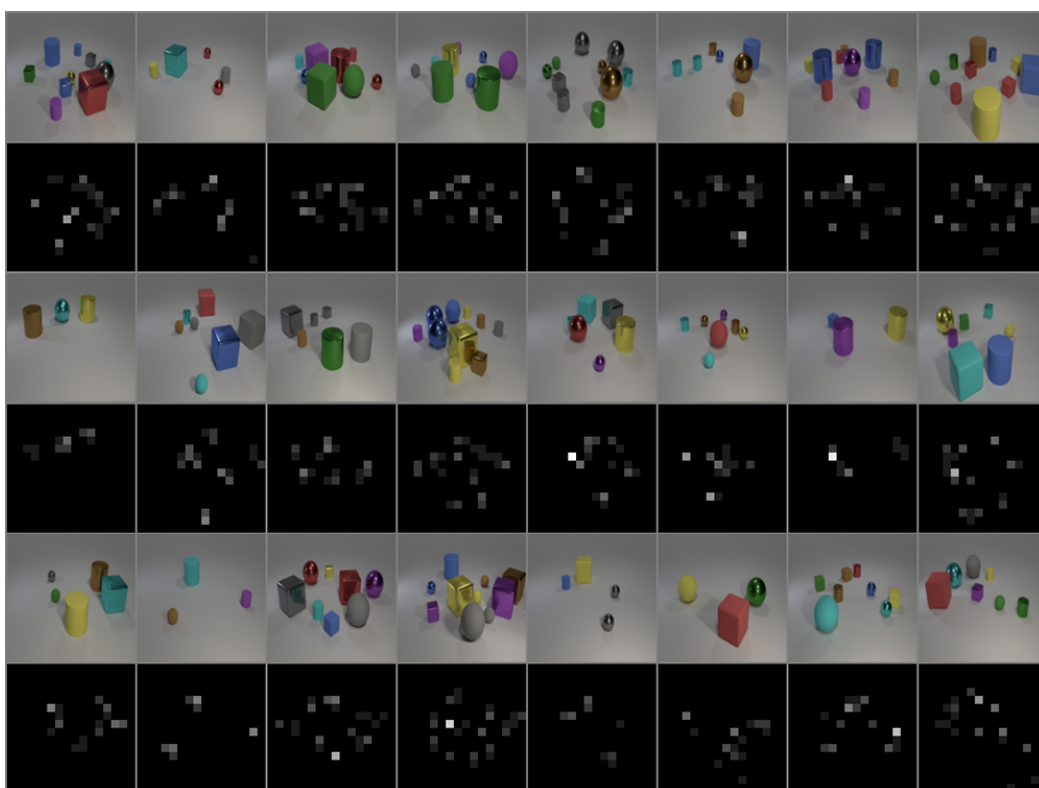


(b) STL-10

Figure 7: Activation Maps for Image Classification tasks. These are the outputs for randomly selected data without manual selection.



(a) Sort of CLEVR



(b) CLEVR

Figure 8: Activation Maps for Relational Reasoning tasks. These are the outputs for randomly selected data without manual selection.